Composites Part B 174 (2019) 107005

Contents lists available at ScienceDirect

Composites Part B

journal homepage: www.elsevier.com/locate/compositesb

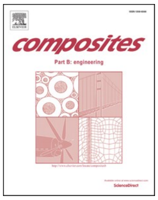

Viscoelastic damage behavior of fiber reinforced nanoparticle-filled epoxy nanocomposites: Multiscale modeling and experimental validation

Behrouz Arash [a,*], Wibke Exner [b], Raimund Rolfes [a]

[a] Institute of Structural Analysis, Leibniz Universität Hannover, Appelstraße 9A, 30167, Hannover, Germany
[b] Institute of Composite Structures and Adaptive Systems, DLR (German Aerospace Center), Lilienthalplatz 7, 38108, Braunschweig, Germany

ARTICLE INFO

Keywords:
Fiber reinforced composite
Nanoparticle
Viscoelastic damage model
Molecular dynamics simulations
Finite element analysis

ABSTRACT

The development of a physically based constitutive model for glass fiber reinforced boehmite nanoparticle-filled epoxy nanocomposites undergoing finite strain is investigated. The constitutive model allows capturing the main features of the stress-strain relationship of the nanocomposites, including the nonlinear hyperelastic, time-dependent and softening behavior. A methodological framework based on molecular dynamics simulations and experimental tests is proposed to identify the material parameters required for the model. The fiber-matrix interaction is characterized by a composite model, which multiplicatively decomposes the deformation gradient into a uniaxial deformation along the fiber direction and a subsequent shear deformation. The effect of the nanoparticles on the stress–strain response is taken into account through the adoption of a modulus enhancement model. The Eyring model parametrized using molecular simulations is used to describe the rate-dependent viscoelastic deformation under loading. The stress softening behavior is captured by a monotonically increasing function of deformation, so-called softening variable. The results show that the model predictions of stress-strain relationships are in good agreement with experimental data at different fiber and nanoparticle weight fractions. Finally, the constitutive model is implemented in the finite element analysis and examined by means of a benchmark example. Experimental–numerical validation confirms the predictive capability of the present modeling framework, which provides a suitable tool for analyzing fiber reinforced nanoparticle/epoxy nanocomposites.

1. Introduction

Materials science is expected to produce major breakthrough discoveries in the coming decades to meet the increasing technological need for more resistant yet lightweight materials used under extreme thermomechanical loading conditions. Continuing research activity concentrating in the field of synthetic composites has promised to develop a class of high-performance glass fiber (GF) reinforced epoxy composites containing various nanofillers such as nanoparticles and nanotubes [1,2]. The utilization of nanoscale fillers in polymer matrices has two important impacts on their material behavior. Firstly, nanoparticles show uniquely different physical and chemical properties from their bulk counterparts, which is related to having a larger portion of their atoms on the surface. Secondly, the extremely high surface-to-volume ratio of nanoparticles offers more contact surface area that can be 1000 times greater than of micro-sized particles. This allows efficient load transfer from the matrix to the reinforcements that is the key to achieving high-performance materials. Recently, boehmite nanoparticles (BNPs) have shown promising results to improve the material properties of the composites such as the shear strength, shear modulus, compressive strength and fracture toughness [3–5].

Although the resulting fiber reinforced BNP/epoxy nanocomposites have proven to be suitable for different engineering applications, the prediction of their mechanical behavior under different loading conditions has become a real challenge. This is mainly due to the nonlinear stress-strain behavior of the nanocomposites resulting not only from external factors (such as strain rate and temperature), but also from microstructural parameters (such as the fiber and nanoparticle weight fractions). A typical stress-strain relationship of the nanocomposites under tensile loading can be divided into three distinct stages: (1) an initially linear increase of stress with stain, (2) a nonlinear behavior due to the presence of nonlinear viscoelasticity and hyperelasticity at higher strains, and (3) a decrease in stress after the stress peak value by increasing strain. The softening behavior may be originated from

---

* Corresponding author.
E-mail addresses: b.arash@isd.uni-hannover.de (B. Arash), wibke.exner@dlr.de (W. Exner), r.rolfes@isd.uni-hannover.de (R. Rolfes).

https://doi.org/10.1016/j.compositesb.2019.107005
Received 5 February 2019; Received in revised form 16 May 2019; Accepted 30 May 2019

irreversible phenomena, such as cavitation and chain scission, which leads the stress reduction in the softening stage [6]. Considering the complex material behavior, a predictive constitutive model that is able to accurately capture the thermomechanical viscoelastic behavior of the nanocomposites is indispensable to predict the stress-strain relationships.

In oder to rationalize the viscoelastic behavior of epoxy resins and their composites, a number of material models have been proposed in the literature to quantitatively capture experimental data [7–12]. Basically, the models can be divided into physically and phenomenologically based constitutive models. In the phenomenological approach, a mathematical model with a set of parameters is defined for materials with similar behavior to fit experimental results. However, the optimum number of the parameters and their physical interpretation are missing since the underlying physical mechanisms at micro-scale do not enter the parameters. Despite the inherent limitations of phenomenological models, due to the complexity of the material behavior of reinforced epoxy resins and the lack of deep physical insights into their deformation mechanisms at the micro-scale, some authors proposed purely phenomenological models [13–18].

To improve on this, physically based constitutive models can play an important role in the development of material models by (1) exploring the relationships between stresses and deformations at the micro-scale, (2) adding new physical insights into mechanisms at molecular level and (3) removing unnecessary assumptions. The physically based constitutive models can offer a systematic material parameters identification since they are able to extrapolate outside of the range of direct experimental validation. Up to now, some studies have been conducted to develop physically based constitutive models for polymers by taking into account their microstructures [19–25]. Van Dommelen et al. [21] proposed a constitutive model for the viscoelastic-viscoplastic deformation of semi-crystalline polymers in which the material is modeled as an aggregate of two-phase layered composite inclusions. In their idealized model, each crystalline lamella is mechanically coupled to its corresponding amorphous layer by enforcing compatibility and traction equilibrium at the interface. An alternative representation of the microstructure based on composite-type formulations was proposed by Boyce et al. [19] and later developed by Ahzi et al. [22] and Ayoub et al. [24], in which the degree of crystallinity is explicitly introduced in the formulations. In the model, the stress-strain behavior is described by two resistances to deformation: (1) an intermolecular barrier that is further amplified by the of strain-induced crystallization; and (2) an evolving anisotropic resistance due to molecular orientation. On the basis of the model, Qi and Boyce [23] developed a constitutive model capturing the main features of the material behavior of semi-crystalline polymers, including the nonlinear hyperelastic behavior, time dependence, hysteresis and stain-induced softening. The constitutive model decomposes the stress-strain behavior into rate-independent equilibrium and rate-dependent viscoelastic–plastic parts. Miehe and Göktepe [26] borrowed the concepts of the tube model to develop a constitutive model for finite strain viscoelasticity of rubber-like materials. They assumed that the rate-dependent response of rubbery polymers is driven by micro-kinematical mechanisms related to the stretch and the area contraction of a tube containing a prototype chain. Li et al. [27] proposed a physically based constitutive model to capture the finite strain viscoelastic behavior of elastomers by decomposing the elastomers into a cross-linked network with superimposed free chains. A procedure based on molecular dynamics (MD) simulations and experimental tests were developed to identify the material parameters.

Although constitutive models with physically motivated derivations exit in the literature, the models usually contain a large number of material parameters that are difficult to derive from the mechanical behavior or from considerations of the microstructure of the polymer network. A unique identification of the parameters for a wide range of loading conditions (e.g., strain rate and temperature) often requires very sophisticated and complicated experimental setups, which make the identification process unfeasible. In most cases, the determination of the material parameters is oversimplified to a curve fitting problem based on the minimization of differences between model results and experimental data, regardless of the uniqueness and the physical meaning of the parameters. Furthermore, the effect of fiber and nanoparticle contents on the stress-strain relationship of cross-linked amorphous polymers has not been considered in the models. In this view, the development of a framework based on molecular simulations and experiments is of great practical value to (1) explore the deformation mechanisms at the molecular level, (2) deterministically predict the material parameters and (3) limit the number of experimental tests required for material parameters identification.

In this study, to tackle the viscoelastic damage behavior of fiber reinforced BNP/epoxy nanocomposites, we present a physically based constitutive model, which accurately captures the nonlinear hyperelastic, time-dependent and softening behavior of the nanocomposites under finite strain (Section 2). In seeking a robust identification procedure, a methodological framework developed based on MD simulations and experimental tests for predicting the material parameters is proposed. Within this framework, MD simulations are performed to investigate the time-independent equilibrium and rate-dependent viscoelastic behavior of the epoxy matrix (Section 3). Molecular simulations of the epoxy resin under tensile loading at various strain rates enable the identification of viscoelastic material parameters. The long-term stress relaxation of the epoxy under a constant shear strain is also investigated using MD simulations by which the material parameters associated with the time-independent response are obtained. Furthermore, the softening parameter is measured by experiments because of the lack of exact knowledge about the mechanism of damage in the nanocomposites. A composite model, which multiplicatively decomposes the deformation gradient into a uniaxial deformation along the fiber direction and a subsequent shear deformation, is adopted to characterize the fiber-matrix interaction. A modulus enhancement model is also used to account for the effect of BNP content on the material behavior. Finally, the constitutive model is implemented in a nonlinear incremental finite element analysis (FEA) to evaluate its applicability in real applications (Section 4). The predictive capability of the constitutive model is validated by comparing the simulation results of uniaxial tensile and four-point bending tests at room temperature with those of experimental data. The numerical results highlight the efficiency and accuracy of the proposed model.

The present study offers a deterministic method to identify the material parameters required to capture the stress-strain behavior of fiber reinforced nanoparticle-filled epoxy nanocomposites. All the parameters are directly obtained from molecular simulations or measured by experimental tests. Beyond this, the present study may have a broad impact on the constitutive modeling of nanocomposites, in the sense that the proposed framework can be extended to other types of reinforced polymer nanocomposites.

2. Constitutive modeling of fiber reinforced nanocomposites

In the following section, we propose a viscoelastic damage constitutive model for the GF-reinforced BNP/epoxy nanocomposites. A composite-based hyperelastic constitutive model previously introduced in the literature [28,29] is first presented to construct an appropriate expression for the strain energy stored in the fiber reinforced composites, and to consider the fiber-matrix interaction. The model is then used to develop a viscoelastic damage model for the nanocomposites. Next, a procedure for identifying the material parameters for the constitutive model is outlined.

2.1. Strain energy for fiber reinforced composites

It has been shown that a multiplicative decomposition of the deformation gradient can be used to construct the strain energy function for transversely isotropic fiber reinforced composites [28–30]. The key concept is to decompose the deformation gradient into uniaxial deformation along the fiber direction and a subsequent shear deformation. Here, we briefly present the development of a strain energy for fiber reinforced composites.

A macroscopic deformation gradient $\mathbf{F}$ contains a volumetric portion that can be taken out through $\overline{\mathbf{F}} = J^{-1/3}\mathbf{F}$, where $J = \det[\mathbf{F}]$. Let $\mathbf{a}_0$ be the original fiber direction. After the deformation $\overline{\mathbf{F}}$, the deformed fiber direction $\overline{\mathbf{F}}\mathbf{a}_0$ can be rotated back to the original fiber direction by rigid body rotations defined by a new deformation gradient $\overline{\mathbf{F}}^*$. Since only rigid body rotations are involved, we therefore have [28].

$$\overline{\mathbf{C}} = \overline{\mathbf{F}}^T\overline{\mathbf{F}} = \overline{\mathbf{F}}^{*^T}\overline{\mathbf{F}}^*. \tag{1}$$

As shown in Ref. [28], the deformation gradient $\overline{\mathbf{F}}^*$ can be multiplicatively decomposed into a uniaxial deformation along the fiber direction $\overline{\mathbf{F}}_f^*$ and a shear deformation $\overline{\mathbf{F}}_s^*$ as

$$\overline{\mathbf{F}}^* = \overline{\mathbf{F}}_f^*\overline{\mathbf{F}}_s^*, \tag{2}$$

where

$$\overline{\mathbf{F}}_f^* = \mathrm{diag}\left[\lambda_F \quad \lambda_F^{-1/2} \quad \lambda_F^{-1/2}\right], \tag{3a}$$

$$\overline{\mathbf{F}}_s^* = \begin{bmatrix} 1 & \overline{F}_{12}^*\lambda_F^{1/2} & \overline{F}_{13}^*\lambda_F^{1/2} \\ 0 & 1 & \overline{F}_{23}^*\lambda_F^{1/2} \\ 0 & 0 & 1 \end{bmatrix}, \tag{3b}$$

and $\lambda_F = |\overline{\mathbf{F}}\mathbf{a}_0|$ represents the stretch of the fiber.

The strain energy of a fiber reinforced composite can be developed using the described decomposition as

$$\psi(\overline{I}_1, \overline{I}_2, \overline{I}_4, \overline{I}_5) = \psi_f(\overline{I}_1, \overline{I}_4) + \psi_s(\overline{I}_1, \overline{I}_4, \overline{I}_5), \tag{4}$$

where ψ_f and ψ_s are the strain energy terms of the composite associated with the uniaxial deformation along the fiber direction $\overline{\mathbf{F}}_f^*$ and the shear deformation $\overline{\mathbf{F}}_s^*$. $\overline{I}_1$, $\overline{I}_2$, $\overline{I}_4$ and $\overline{I}_5$ are defined as

$$\begin{aligned} \overline{I}_1 &= \mathrm{tr}\left[\overline{\mathbf{C}}\right], \\ \overline{I}_2 &= \frac{1}{2}\left(\left(\mathrm{tr}\left[\overline{\mathbf{C}}\right]\right)^2 - \mathrm{tr}\left[\overline{\mathbf{C}}^2\right]\right), \\ \overline{I}_4 &= \mathbf{a}_0 \cdot \overline{\mathbf{C}} \cdot \mathbf{a}_0, \\ \overline{I}_5 &= \mathbf{a}_0 \cdot \overline{\mathbf{C}}^2 \cdot \mathbf{a}_0 \end{aligned} \tag{5}$$

The strain energy stored in the composite during the deformation $\overline{\mathbf{F}}_f^*$ is given by

$$\psi_f = \psi_f^M + \psi_f^F = \frac{1}{2}\nu_M\mu_M\left[\overline{I}_1\left(\overline{\mathbf{F}}_f^*\right) - 3\right] + \frac{1}{2}\nu_F\mu_M f\left(\overline{I}_4\right)\left[\overline{I}_1\left(\overline{\mathbf{F}}_f^*\right) - 3\right], \tag{6}$$

where ν_M and ν_F are respectively the matrix and fiber volume fractions ($\nu_M + \nu_F = 1$). $\overline{I}_1(\overline{\mathbf{F}}_f^*) = \lambda_F^2 + \frac{2}{\lambda_F} = \overline{I}_4 + 2\overline{I}_4^{-1/2}$ is the first invariant of the tensor $\mathbf{C}_f^* = \mathbf{F}_f^{*^T}\mathbf{F}_f^*$. μ_M is the shear modulus of the matrix, and $f(\overline{I}_4)$ represents the stiffness ratio between the fiber and the matrix prescribed to be [29].

$$f\left(\overline{I}_4\right) = a_1 + a_2 \exp\left[a_3\left(\overline{I}_4 - 1\right)\right], \tag{7}$$

where a_1, a_2 and a_3 are positive parameters, which are determined through a calibration process discussed later.

An expression for the strain energy stored in the composite during the shear deformation $\overline{\mathbf{F}}_s^*$ is given by

$$\psi_s = \frac{1}{2}\mu_C\left[\overline{I}_1 - \overline{I}_1\left(\overline{\mathbf{F}}_f^*\right)\right], \tag{8}$$

where μ_C is the effective shear modulus of the composite obtained using the Halpin-Tsai micromechanics based equations [31] as

$$\frac{\mu_C}{\mu_M} = \frac{1 + \zeta\eta\nu_F}{1 - \eta\nu_F}, \tag{9}$$

To extend the equation to the large deformation, η can be calculated from

$$\eta = \frac{f\left(\overline{I}_4\right) - 1}{f\left(\overline{I}_4\right) + \zeta}, \tag{10}$$

in which

$$\zeta = \begin{cases} 1 & \text{in} - \text{plane shear} \\ 0.4 & \text{transverse shear} \end{cases}. \tag{11}$$

Considering Eqs. (9) and (10), the strain energy under shear deformation can rewritten as

$$\psi_s = \frac{1}{2}\mu_M g\left[f\left(\overline{I}_4\right), \nu_F, \zeta\right]\left[\overline{I}_1 - \overline{I}_1\left(\overline{\mathbf{F}}_f^*\right)\right], \tag{12}$$

where

$$g\left[f\left(\overline{I}_4\right), \nu_f, \zeta\right] = \frac{\mu_C}{\mu_M} = \frac{(1 + \zeta\nu_F)f\left(\overline{I}_4\right) + (1 - \nu_F)\zeta}{(1 - \nu_F)f\left(\overline{I}_4\right) + (\zeta + \nu_F)}. \tag{13}$$

and

$$\overline{I}_1 - \overline{I}_1\left(\overline{\mathbf{F}}_f^*\right) = \frac{\overline{I}_5 - \overline{I}_4^2}{\overline{I}_4} + \overline{I}_1 - \frac{\overline{I}_5 + 2\sqrt{\overline{I}_4}}{\overline{I}_4}. \tag{14}$$

The strain energy function derived for a fiber reinforced composite in Eq. (4) can be homogenized for a composite with N number of families of fiber reinforcements illustrated in Fig. 1. Let $\mathbf{a}_0^i$ be the unit vector denoting the original direction of the family of fibers i with the volume fraction ν_i ($\nu_F = \sum_{i=1}^{N}\nu_F^i$). The homogenized strain energy function is then the sum of the strain energies for the N families of fibers, i.e.,

$$\psi^t = \frac{1}{\nu_F}\sum_{i=1}^{N}\nu_F^i\psi^i, \tag{15}$$

where

$$\begin{aligned} \psi^i = &\frac{1}{2}\nu_M\mu_M\left[\overline{I}_1\left(\overline{\mathbf{F}}_f^{*i}\right) - 3\right] + \frac{1}{2}\nu_F\mu_M f\left(\overline{I}_4^i\right)\left[\overline{I}_1\left(\overline{\mathbf{F}}_f^{*i}\right) - 3\right] \\ &+ \frac{1}{2}\mu_M g\left[f\left(\overline{I}_4^i\right), \nu_F, \zeta\right]\left[\overline{I}_1 - \overline{I}_1\left(\overline{\mathbf{F}}_f^{*i}\right)\right]. \end{aligned} \tag{16}$$

In the formula above, the fiber–fiber interaction is eliminated to simplify the constitutive model.

2.2. Viscoelastic damage constitutive model

To rationalize the viscoelastic behavior of fiber reinforced nanoparticle/epoxy nanocomposites, their stress response is decomposed into a hyperelastic (time-independent equilibrium) part and a viscous

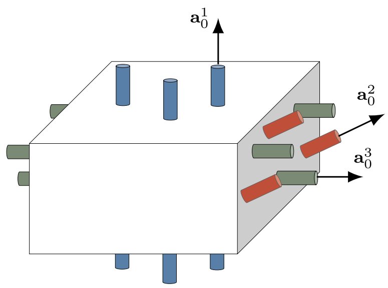

Fig. 1. Schematic of a composite with a number of families of fiber reinforcements.

part (rate-dependent non-equilibrium). The time-independent equilibrium part of the stress–strain behavior, comprising of a hyperelastic rubbery spring, is associated with the entropy change of the polymer network due to deformation. The rate-dependent non-equilibrium part consists of a nonlinear spring characterizing the initial elastic contribution due to internal energy change, and a nonlinear viscoplastic dashpot capturing the rate and temperature dependent behavior of the material (see Fig. 2). The elastic behavior is assumed to originate from the connectivity and stretching of the polymer network and interactions between fiber and nanoparticle reinforcements, and polymer chains. In contrast, the viscous behavior is taken to be governed by frictional interactions between polymer chains. The rate-dependent non-equilibrium part tends to relax the elastic deformation and hence produces the relaxation of the stress–strain behavior to the equilibrium path with time. In addition, the viscoplastic behavior of the nanocomposites comes from different energy dissipation sources during deformation, including the breakage of bonds and interactions between polymer and nanoparticle [23]. The quasi-irreversible rearrangements of microstructures result in stress softening in the material known as Mullins effect [32,33].

A constitutive model for the finite deformation viscoelastic damage behavior of the composite polymer should be able to capture four main features of the material behavior. The features are (1) the nonlinear elastic behavior under large deformation, (2) the time dependent material response, (3) softening of the equilibrium paths during deformation, and (4) the effect of fiber and nanoparticle content on the mechanical properties. The model is detailed in the following section.

The total deformation gradient $\mathbf{F}_t$ in viscoelasticity is determined from an exploitation of the multiplicative decomposition as [34].

$$\mathbf{F}_t = \mathbf{F}_e \mathbf{F}_v, \tag{17}$$

where $\mathbf{F}_e$ represents the elastic portion of the motion and $\mathbf{F}_v$ is associated with the inelastic motion of the material.

The overall free energy of the material can be decomposed into an equilibrium and a non-equilibrium part, i.e.,

$$\Psi(\mathbf{C}_t, \mathbf{F}_v, d) = (1-d)\left[\Psi_{eq}(\mathbf{C}_t) + \Psi_{neq}\left(\mathbf{F}_v^{-T}\mathbf{C}_t\mathbf{F}_v^{-1}\right)\right], \tag{18}$$

where $d \in [0, 1)$ is a scalar damage variable with initial condition $d = 0$ and $\mathbf{C}_t = \mathbf{F}_t^T \mathbf{F}_t$.

From the second law of thermodynamics, the Clausius-Duhem inequality for an isothermal process can be written as

$$\Phi = -\dot{\Psi} + \frac{1}{2}\mathbf{S} : \dot{\mathbf{C}}_t \geq 0 \tag{19}$$

where $\mathbf{S}$ is the second Piola-Kirchhoff stress tensor. The rate of free energy then takes the form

$$\dot{\Psi} = \frac{\partial \Psi}{\partial \mathbf{C}_t} : \dot{\mathbf{C}}_t + \frac{\partial \Psi}{\partial \mathbf{F}_v} : \dot{\mathbf{F}}_i + \frac{\partial \Psi}{\partial d} : \dot{d} \tag{20}$$

by which the dissipation inequality Eq. (19) reduces to

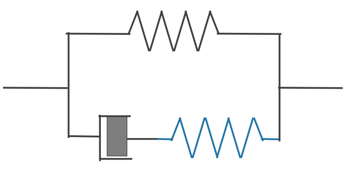

Fig. 2. One-dimensional schematic of the constitutive model of a hyperelastic spring in parallel with a viscoelastic component that consist of a nonlinear elastic spring and a nonlinear viscoplastic dashpot.

$$\begin{aligned}\Phi = &\left(\mathbf{S} - 2(1-d)\frac{\partial \Psi_{eq}}{\partial \mathbf{C}_t} - 2(1-d)\mathbf{F}_v^{-1}\frac{\partial \Psi_{neq}}{\partial \mathbf{C}_e}\mathbf{F}_v^{-T}\right) : \frac{1}{2}\dot{\mathbf{C}}_t \\ &-(1-d)\frac{\partial \Psi_{neq}}{\partial \mathbf{C}_e} : \frac{\partial \mathbf{C}_e}{\partial \mathbf{F}_v} : \dot{\mathbf{F}}_v + \frac{\partial(\Psi)}{\partial d}\dot{d} \geq 0,\end{aligned} \tag{21}$$

where $\mathbf{C}_e = \mathbf{F}_v^{-T}\mathbf{C}\mathbf{F}_v^{-1}$.

By substituting the assumed functional form Eq. (20) into Eq. (19), the stress can be split into an equilibrium contribution and a non-equilibrium contribution as [34].

$$\mathbf{S} = (1-d)\left[\underbrace{2\frac{\partial \Psi_{eq}}{\partial \mathbf{C}_t}}_{\mathbf{S}_{eq}} + \underbrace{2\mathbf{F}_v^{-1}\frac{\partial \Psi_{neq}}{\partial \mathbf{C}_e}\mathbf{F}_v^{-T}}_{\mathbf{S}_{neq}}\right]. \tag{22}$$

The following terms remain in the dissipation inequality

$$\Phi = \underbrace{2(1-d)\mathbf{C}_e\frac{\partial \Psi_{neq}}{\partial \mathbf{C}_e} : \mathbf{L}_v}_{\Phi_v} + \underbrace{\frac{\partial(\Psi)}{\partial d}\dot{d}}_{\Phi_d} \geq 0, \tag{23}$$

where $\mathbf{L}_v$ is the velocity gradient of the relaxed configuration given by $\mathbf{L}_v = \dot{\mathbf{F}}_v\mathbf{F}_v^{-1}$. Here, we assume that Φ_v and Φ_d are independently positive.

To proceed further, we first introduce a viscoelastic damage model for the nanoparticle reinforced epoxy composites. The proposed constitutive equations can be interpreted as a parallel type rheological model with a Maxwell element in parallel with an equilibrium spring as illustrated in Fig. 2. As mentioned earlier, the constitutive model consists of three elements: (1) A hyperelastic spring, (2) a nonlinear elastic spring, and (3) a nonlinear viscoplastic dashpot. Here, we use the generalized neo-Hookean model for fiber reinforced composites presented in Eqs. (15) and (16) for the equilibrium and non-equilibrium free energy terms as

$$\begin{aligned}\Psi_{eq} &= \frac{1}{\nu_F}\sum_{i=1}^{N}\nu_F^i\Psi_{eq}^i, \\ \Psi_{eq}^i &= \frac{1}{2}\nu_M X\mu_M^e\left[\bar{I}_{t_1}\left(\overline{\mathbf{F}}_{tf}^{*i}\right) - 3\right] + \frac{1}{2}\nu_F X\mu_M^e f\left(\bar{I}_{t_4}^i\right)\left[\bar{I}_{t_1}\left(\overline{\mathbf{F}}_{tf}^{*i}\right) - 3\right] \\ &+ \frac{1}{2}X\mu_M^e g\left[f\left(\bar{I}_{t_4}^i\right), \nu_F, \zeta\right]\left[\bar{I}_{t_1} - \bar{I}_{t_1}\left(\overline{\mathbf{F}}_{tf}^{*i}\right)\right],\end{aligned} \tag{24}$$

and

$$\begin{aligned}\Psi_{neq} &= \frac{1}{\nu_F}\sum_{i=1}^{N}\nu_F^i\Psi_{neq}^i + \frac{1}{2}\lambda_M^v(J^e - 1)^2, \\ \Psi_{neq}^i &= \frac{1}{2}\nu_M X\mu_M^v\left[\bar{I}_{e_1}\left(\overline{\mathbf{F}}_{ef}^{*i}\right) - 3\right] + \frac{1}{2}\nu_F X\mu_M^v f\left(\bar{I}_{e_4}^i\right)\left[\bar{I}_{e_1}\left(\overline{\mathbf{F}}_{ef}^{*i}\right) - 3\right] \\ &+ \frac{1}{2}X\mu_M^v g\left[f\left(\bar{I}_{e_4}^i\right), \nu_F, \zeta\right]\left[\bar{I}_{e_1} - \bar{I}_{e_1}\left(\overline{\mathbf{F}}_{ef}^{*i}\right)\right],\end{aligned} \tag{25}$$

where the superscript i denotes the ith family of fibers, μ_M^e is the shear moduli respectively related to the equilibrium response of the polymer matrix, and μ_M^v and λ_M^v are the Lamé moduli associated with the non-equilibrium response of the matrix. $\bar{I}_{t_1}$, $\bar{I}_{e_1}$, J^e are also defined as

$$\begin{aligned}&\bar{I}_{t_1} = J_t^{-2/3}\mathrm{tr}[\mathbf{C}_t],\ \bar{I}_{t_4}^i = J_t^{-2/3}\mathbf{a}_0^i \cdot \mathbf{C}_t \cdot \mathbf{a}_0^i, \\ &\bar{I}_{e_1} = J_e^{-2/3}\mathrm{tr}[\mathbf{C}_e],\ \bar{I}_{e_4}^i = J_e^{-2/3}\mathbf{a}_0^i \cdot \mathbf{C}_e \cdot \mathbf{a}_0^i, \\ &J_t = \det[\mathbf{F}_t],\ \mathbf{C}_t = \mathbf{F}_t^T\mathbf{F}_t, \\ &J_e = \det[\mathbf{F}_e],\ \mathbf{C}_e = \mathbf{F}_e^T\mathbf{F}_e.\end{aligned} \tag{26}$$

In order to take into account the effect of nanoparticles, the moduli are multiplied by an amplification factor X, which depends on the nonoparticle volume fraction. Following the earlier work of Guth [35], X takes a form of $X = 1 + 2.5\nu_{np} + 14.1\nu_{np}^2$ for rigid nanoparticles, where ν_p represents the nanoparticle volume fraction.

The total Cauchy stress is thus given by

$$\mathbf{T}=(1-d)\left(\mathbf{T}_{eq}+\mathbf{T}_{neq}\right), \tag{27}$$

where $\mathbf{T}_{eq}$ and $\mathbf{T}_{neq}$ are the portions of the total stress originating from the hyperelastic rubbery and the viscoelastic behavior of the material, respectively. The stresses are finally expressed as

$$\begin{aligned}\mathbf{T}_{eq}=&\frac{2}{J_t}\sum_{i=1}^{N}\left[\frac{\partial\Psi^i_{eq}}{\partial\overline{I}_{t_1}}\mathrm{dev}\left[\overline{\mathbf{B}}_t\right]+\frac{\partial\Psi^i_{eq}}{\partial\overline{I}^i_{t_4}}\overline{I}^i_{t_4}\left(\mathbf{a}^i_e\otimes\mathbf{a}^i_e-\frac{1}{3}\mathbf{I}\right)\right.\\&\left.+\frac{\partial\Psi^i_{eq}}{\partial\overline{I}^i_{t_5}}\left(\overline{I}^i_{t_4}\left(\mathbf{a}^i_e\otimes\overline{\mathbf{B}}_t\cdot\mathbf{a}^i_e+\mathbf{a}^i_e\cdot\overline{\mathbf{B}}_t\otimes\mathbf{a}^i_e\right)-\frac{2}{3}\overline{I}^i_{t_5}\mathbf{I}\right)\right],\end{aligned} \tag{28}$$

and

$$\begin{aligned}\mathbf{T}_{neq}=&\frac{2}{J_e}\sum_{i=1}^{N}\left[\frac{\partial\Psi^i_{neq}}{\partial\overline{I}_{e_1}}\mathrm{dev}\left[\overline{\mathbf{B}}_e\right]+\frac{\partial\Psi^i_{neq}}{\partial\overline{I}^i_{e_4}}\overline{I}^i_{e_4}\left(\mathbf{a}^i_v\otimes\mathbf{a}^i_v-\frac{1}{3}\mathbf{I}\right)\right.\\&\left.+\frac{\partial\Psi^i_{neq}}{\partial\overline{I}^i_{e_5}}\left(\overline{I}^i_{e_4}\left(\mathbf{a}^i_v\otimes\overline{\mathbf{B}}_e\cdot\mathbf{a}^i_v+\mathbf{a}^i_v\cdot\overline{\mathbf{B}}_e\otimes\mathbf{a}^i_v\right)-\frac{2}{3}\overline{I}^i_{e_5}\mathbf{I}\right)\right]+\frac{\partial\Psi_{neq}}{\partial J_e}\mathbf{I},\end{aligned} \tag{29}$$

where $\overline{\mathbf{B}}_t=\overline{\mathbf{F}}_t\overline{\mathbf{F}}_t^T$ and $\overline{\mathbf{B}}_e=\overline{\mathbf{F}}_e\overline{\mathbf{F}}_e^T$ are the isochoric left Cauchy–Green tensor related to the equilibrium and non-equilibrium responses, respectively. $\mathbf{a}^i_v=\frac{\overline{\mathbf{F}}_e\mathbf{a}^i_0}{\sqrt{\overline{I}^i_{e_4}}}$, $\mathbf{a}^i_e=\frac{\overline{\mathbf{F}}_t\mathbf{a}^i_0}{\sqrt{\overline{I}^i_{t_4}}}$ are the current fiber directions associated with the equilibrium and non-equilibrium responses, respectively. $\mathbf{I}$ is the second order unit tensor, and $\frac{\partial\Psi^i}{\partial\overline{I}_j}$ $(j=1,\ 4\ \text{and}\ 5)$ can be calculated as follows:

$$\begin{aligned}&\frac{\partial\Psi^i}{\partial\overline{I}_1}\left(\overline{I}^i_4,\mu_M\right)=\frac{1}{2}g\left[f\left(\overline{I}^i_4\right),\nu_F,0.4\right]\mu_M,\\&\frac{\partial\Psi^i}{\partial\overline{I}_4}\left(\overline{I}_1,\overline{I}^i_4,\overline{I}^i_5,\mu_M\right)=\frac{1}{2}\mu_M\left[\nu_F\frac{\partial f\left(\overline{I}^i_4\right)}{\partial\overline{I}^i_4}\left(\overline{I}^i_4+2\overline{I}_4^{i^{-1/2}}-3\right)+\left(\nu_M+\nu_F f\left(\overline{I}^i_4\right)\right)\left(1-\overline{I}_4^{i^{-3/2}}\right)\right.\\&-g\left[f\left(\overline{I}^i_4\right),\nu_F,1\right]\left(\overline{I}^i_5\overline{I}_4^{i^{-2}}+1\right)+g\left[f\left(\overline{I}^i_4\right),\nu_F,0.4\right]\left(\overline{I}^i_5\overline{I}_4^{i^{-2}}+\overline{I}_4^{i^{-3/2}}\right)\\&\left.+\frac{\overline{I}^i_5-\overline{I}_4^{i^2}}{2\overline{I}^i_4}\frac{\partial g\left[f\left(\overline{I}^i_4\right),\nu_F,0.4\right]}{\partial\overline{I}^i_4}+\frac{1}{2}\left(\overline{I}_1-\frac{\overline{I}^i_5+2\sqrt{\overline{I}^i_4}}{\overline{I}^i_4}\right)\frac{\partial g\left[f\left(\overline{I}^i_4\right),\nu_F,0.4\right]}{\partial\overline{I}^i_4}\right],\\&\frac{\partial\Psi^i}{\partial\overline{I}_5}\left(\overline{I}^i_4,\mu_M\right)=\frac{1}{2\overline{I}^i_4}\left(g\left[f\left(\overline{I}^i_4\right),\nu_F,1\right]-g\left[f\left(\overline{I}^i_4\right),\nu_F,0.4\right]\right)\mu_M.\end{aligned} \tag{30}$$

In above equations $\overline{I}_1=\overline{I}_{t_1},\overline{I}^i_4=\overline{I}^i_{t_4}\,\text{and}\,\overline{I}^i_5=\overline{I}^i_{t_5}$ for the equilibrium response $\mathbf{T}_{eq}$, and $\overline{I}_1=\overline{I}_{e_1},\overline{I}^i_4=\overline{I}^i_{e_4}\,\text{and}\,\overline{I}^i_5=\overline{I}^i_{e_5}$ for the non-equilibrium response $\mathbf{T}_{neq}$.

The velocity gradient of the relaxed configuration, $\mathbf{L}_v=\dot{\mathbf{F}}_v\mathbf{F}_v^{-1}$, may be represented as the sum of symmetric and skew-symmetric tensors,

$$\mathbf{L}_v=\mathbf{D}_v+\mathbf{W}_v, \tag{31}$$

where $\mathbf{D}_v$ and $\mathbf{W}_v$ are the rate of stretching and spin, respectively. The rate of spin is taken to be $\mathbf{W}_v=0$ [36], and the rate of viscoelastic stretching is prescribed to be

$$\mathbf{D}_v=\frac{\dot{\varepsilon}_v}{\tau_{neq}}\mathrm{dev}\left[\mathbf{T}^{`}_{neq}\right], \tag{32}$$

where $\mathbf{T}^{`}_{neq}=\mathbf{R}_e^T\mathbf{T}_{neq}\mathbf{R}_e$ is the stress acting on the viscoelastic component convected to its relaxed configuration. The scalar equivalent stress τ_{neq} is here taken as the Frobenius norm of the deviatoric part of the driving stress $\tau_{neq}=\mathrm{dev}\,[\mathbf{T}_{neq}]_F$. $\dot{\varepsilon}^v$ in Eq. (32) is the viscoelastic flow rate that is defined by the Eyring model [37].

$$\dot{\varepsilon}^v=\dot{\varepsilon}_0\exp\left\{\left[\frac{V^*\tau_{neq}}{k\Theta}\right]\right\}, \tag{33}$$

where $\dot{\varepsilon}_0$ and V^* are respectively pre-exponential factor and the activation volume. As shown in Ref. [34], the evolution equation presented in Eq. (31) satisfies the Clausius-Duhem inequality in Eq. (23) (i.e., $\phi_i\geq 0$).

From Eq. (1), the time-derivative of $\dot{\mathbf{F}}_v$ can be obtained as

$$\dot{\mathbf{F}}_v=\frac{\dot{\varepsilon}^v}{\tau_{neq}}\mathrm{dev}\left[\mathbf{T}^{`}_{neq}\right]\mathbf{F}_v. \tag{34}$$

The evolution of d is assumed to take a simplified form of saturation type evolution rule [38,39], which has the form

$$\dot{d}=A(1-d)\dot{\Lambda}^{max}_{chain}, \tag{35}$$

where A is a parameter that characterizes the evolution of d and

$$\dot{\Lambda}^{max}_{chain}=\begin{cases}0 & \Lambda_{chain}<\Lambda^{max}_{chain}\\ \dot{\Lambda}_{chain} & \Lambda_{chain}\geq\Lambda^{max}_{chain}\end{cases} \tag{36}$$

and $\Lambda_{chain}=\sqrt{\mathrm{tr}[\overline{\mathbf{B}}]/3}$ is the stretch on each chain.

The proposed damage evolution model satisfies the Clausius-Duhem inequality presented in Eq. (23) (i.e., $\Phi_d\geq 0$).

2.3. Summary of the constitutive model

The constitutive model is summarized in Table 1, where parameters required to fully capture each feature of the material behavior are listed.

In the next section, we propose simulation-based procedures for determining the material parameters of the viscoelastic dashpot and hyperelastic spring elements. The procedures provide a methodological framework to extract the material parameters required for the constitutive model. It is worth noting that the evolution of the nanocomposite microstructure due to a quasi-irreversible rearrangement of molecular networks during deformation can cause the softening behavior. Most softening theories are based on two concepts. The first theory, proposed by Blanchard and Parkinson [40] and Bueche [41], considers that the softening behavior results from the breakage or loosening of filler-polymer attachments. The second theory, originated from Mullins and coworkers [32,42], assumes that a quasi-irreversible rearrangement of molecular networks due to localized nonaffine deformation resulting from short chains reaching the limit of their extensibility. This nonaffine deformation produces a displacement of the network junctions from their initial state, which causes the rearrangement of microstructure and the softening behavior. Here, due to the lack of exact information about the morphology of BNP/epoxy nanocomposites at the micro-scale and the mechanism of damage evolution in the materials subjected to loading, the elastic spring and the damage parameters are determined through a calibration process with experimental results. The proposed approach to calibrate the constitutive model and the implementation of the model in a FEA are highlighted in Fig. 3.

Table 1
Summary of the constitutive model and parameters corresponding to each element.

$\mathbf{T}=(1-d)$ $(\mathbf{T}_{eq}+\mathbf{T}_{neq})$	Equilibrium response $\mathbf{T}_{eq}$	Hyperelastic spring element	μ^{he}_M	Eq. (28)
	Non-equilibrium response $\mathbf{T}_{neq}$	Nonlinear spring element	μ^e_M, λ^e_M	Eq. (29)
		Viscoplastic dashpot element	$\dot{\varepsilon}_0$, V^*	Eq. (33)
	Damage		A	Eq. (35)
	Fiber parameters		$a_1, a_2,$ a_3	Eq. (7)

In the multiscale analysis of materials, different length and time scales are involved, which cause many complexities to couple these scales such as size and non-physical effects. Different multiscale methods proposed in literature can be generally classified into hierarchical, semi-concurrent and concurrent methods. Among many others, we refer to studies by Ju and Lee [43], Raghavan and Ghosh [44], and Rabczuk and his colleagues [45–47]. Here, we propose a hierarchical multiscale method, where a numerical homogenization is used to obtain the size-independent material properties from simulations of the microstructure. Meanwhile, the size-dependent damage variable is experimentally identified for specimens at macro-scale, which would prevent from the size effect involved in upscaling the material properties from the fine-scale to the coarse-scale.

3. Molecular simulation based parameters identification

In the following section, a molecular modeling method for simulating the cross-linking process of epoxy resins is first presented. It allows the construction of realistic atomistic models of cured epoxy resins. Next, MD simulations are performed to investigate the material behavior of the cured polymer materials subjected to tensile and shear loading.

3.1. *Curing simulation*

The curing simulations are performed for a commercially available amine-cured epoxy resin combined of two monomers bisphenol a diglycidyl ether and 1,4-butanediol diglycidyl ether with an average weight fraction ratio of 85:15 and an average repeating unit of $n = 1.265$ for bisphenol a diglycidyl ether. The hardeners comprise a combination of poly[oxy(methyl-1,2-ethanediyl)] and cyclohexanemethanamin with an average weight fraction ratio of 62.5:37.5. The number of repeating units for poly[oxy(methyl-1,2-ethanediyl)] is $n = 9.5$. The simulations are conducted on the standard stoichiometric epoxy monomer/hardener ratio of 100:31. The chemical structures of the molecules and the principle polymerisation reactions associated with the cross-linking process are shown in Figs. 4 and 5, respectively.

The monomer and hardener molecules are firstly generated and randomly distributed in a simulation box with the mixing ratio. The total number of atoms is 14974 and periodic boundary conditions are applied along all directions. An optimized molecule arrangement is generated using the open source package PACKMOL [48]. All reactive groups are then activated, as shown in Fig. 6, with the black square indicating a possible covalent bond to a reaction partner. The epoxy group is broken up and the oxygen is hydrated to a hydroxyl group, resulting in an reactive methylene group. Both hydrogen atoms of the amine groups are removed, resulting in a reactive primary amine.

The cross-linking simulation procedure is followed under an isothermal–isobaric ensemble (NPT) with zero external pressure to allow for a sufficient relaxation and to trace the curing-induced volume change:

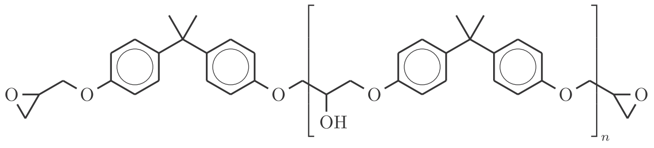
(a) Bisphenol A diglycidyl ether

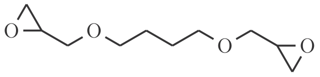
(b) 1,4-Butanediol diglycidyl ether

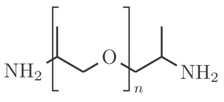
(c) Poly[oxy(methyl-1,2-ethanediyl)]

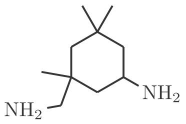
(d) 3-(aminomethyl)-3,5,5-trimethyl-cyclohexanamine

Fig. 4. Chemical structures of all molecules of the investigated epoxy system: (a)–(b) chemical components of epoxy resin monomers, (c)–(d) chemical components of hardener molecules.

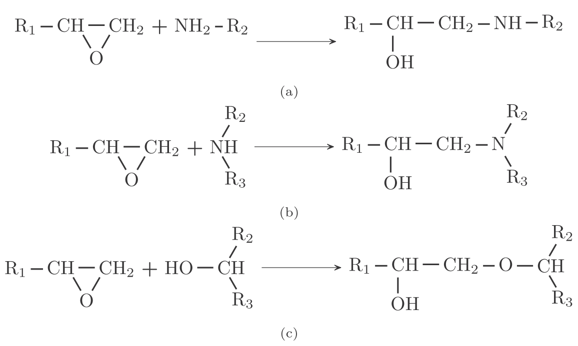

Fig. 5. Principle polymerisation reactions: (a) epoxy group with primary amine, (b) epoxy group with secondary amine, (c) epoxy group with hydroxyl group.

Step 1: An initial relaxation for 500 ps under NPT ensemble combined with a linear increase of temperature to the curing temperature $T = 353$ K;

Step 2: Distances between all possible reactions groups are calculated; all reaction distances larger than a chosen cut-off $r_c = 1$ nm for

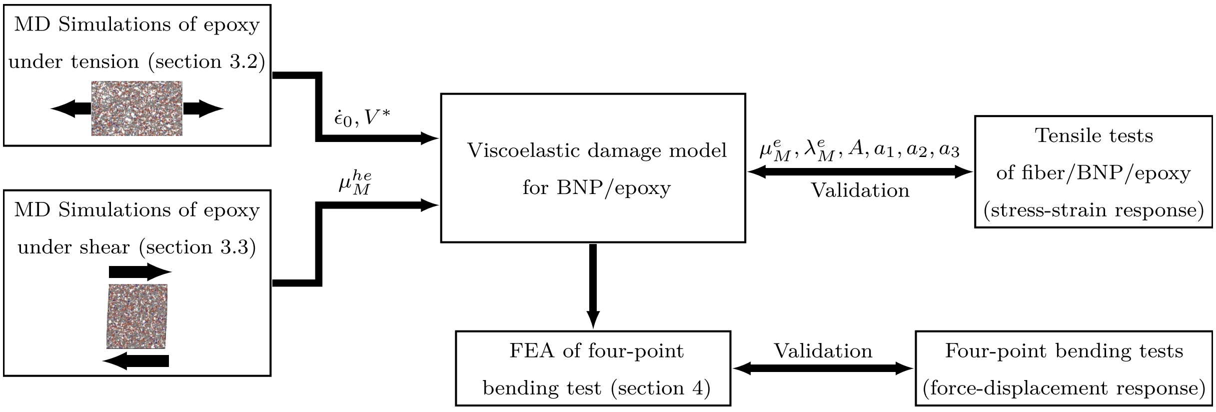

Fig. 3. Summary of the proposed viscoelastic damage constitutive model for fiber reinforced BNP/epoxy nanocomposites.

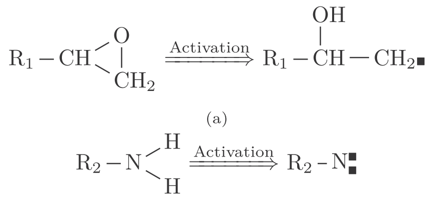

(a)

(b)

Fig. 6. Activation of (a) epoxy group and (b) amine group. A black square (■) indicates a possible covalent bond to a reaction partner.

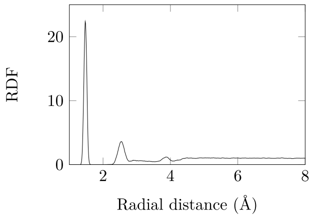

Fig. 8. Radial distribution function of all nitrogen atoms to all carbon atoms in the system.

Table 2
Material parameters predicted by MD simulations.

	Parameter	Equation	Value
Viscoelastic dashpot	$\dot{\varepsilon}_0$ (s^{-1})	(33)	1.43×10^{-7}
	V^* (nm^3)	(33)	0.79
Hyperelastic spring	μ^N (MPa)	(28)	205.50
	N	(28)	2.44

the reaction distance are discarded and the bond with the smallest reaction distance is formed;
Step 3: Equilibration of the system for a time period of 2.5 ps;
Step 4: Repeat step 2 and 3 until the final degree of curing of 90%.

The cross-linking simulations are performed using an in-house code [49]. To study interactions associated with epoxy monomers and hardener molecules, we use the DREIDING force field [50], which is proven to be an appropriate choice for simulations of epoxy systems. The time step is set to be 1 fs. The cross-linking algorithm follows the common approach to use the distance between two reactive groups as the main criterion for an artificial bond formation between the groups. For further information, the reader is referred to Unger et al. [51].

Fig. 7a shows the time evolution of the degree of curing during the cross-linking simulations described in Section 3.1. The simulation results show that the investigated epoxy system is fully cross-linked after a reasonable cross-linking time of about 2 ns (i.e., the degree of cross-linking is greater than 90%). The relative change of reactive amine groups as a function of the degree of curing is also presented in Fig. 7b. The increase of tertiary amine groups by increasing the degree of cross-linking confirms the artificial carbon-nitrogen bond formation associated with the curing simulations. For further analysis, the radial distribution function (RDF) of all nitrogen atoms to all other carbon atoms in the polymer network is shown in Fig. 8. The RDF depicts the main peak at the equilibrium distance of the carbon-nitrogen bond, proving that the system is cross-linked and is at a well equilibrium state.

The simulations are repeated to generate three cross-linked epoxy samples. Next, an NPT simulation at 300 K and 1 bar is conducted for 20 ns for each sample, and two configurations are extracted for the subsequent analysis every 5 ns during the last 10 ns of the simulation. Finally, six cross-linked epoxy samples are prepared. The average number of rigid links between two cross-links represented by N in Eq. (28) is obtained to be 2.44 for the cured epoxy resins as presented in Table 2.

3.2. Modeling of cured epoxy under tensile loading

Once the cured samples are prepared, they are independently subjected to tensile deformations along the $x-$, $y-$, and $z-$ directions at various strain rates and room temperature $T = 298$ K. A 40% axial tensile strain is applied to the periodic polymer system with zero-valued pressures in the lateral directions to allow for the natural Poisson contraction. The simulations of the cured epoxy subjected to tensile loading enables us to study the rate-dependent viscoelastic behavior of the material. The characterization of the viscoelastic flow rate of the epoxy resin will be possible through the analysis of the simulation results along with the Eyring model presented in Eq. (33). Based on the transition state theory, Eyring [52] showed that the deformation of a polymer is a thermally activated process involving the motion of segments of chain molecules over energy barriers. An external applied stress or strain allows a molecule rearrangement to an more energy-efficient state by providing the necessary energy to overcome the energy barrier. The pre-exponential factor and the activation volume required in model are then obtained from the resulting Eyring plot.

A representative stress–strain curve of the cured epoxy system at strain rate $\dot{\varepsilon} = 1 \times 10^8$ s^{-1} is shown in Fig. 9. The simulation data points are fitted by a piecewise cubic spline interpolation with an optimized knot. The knot point $(1/T_k)$ of the bicubic fit is determined by minimizing the least square error between the fit and the simulation data. The maximum observed on the stress–strain curve, which is the yield point, has been marked by an arrow in the figure. The yield point is associated with a sudden increase in the amount of strain which relaxes the stress. From Fig. 9, the yield stress at the strain rate equal to 1×10^8 s^{-1} is calculated to be 282.27 MPa.

An estimation of the viscoelastic flow rate can be obtained from the Eyring plot according to Eq. (33). For this, the deviatoric part of the yield stress (dev $[\sigma_Y]$) at multiple strain rates varying from 5×10^6 to 5×10^8 s^{-1} is calculated. The resulting Eyring plot shown in Fig. 10 suggest a linear behavior from which the preexponential factor and the activation volume are obtained to be 1.43×10^{-7} s^{-1} and 0.79 nm^3, respectively. The values are listed in Table 2.

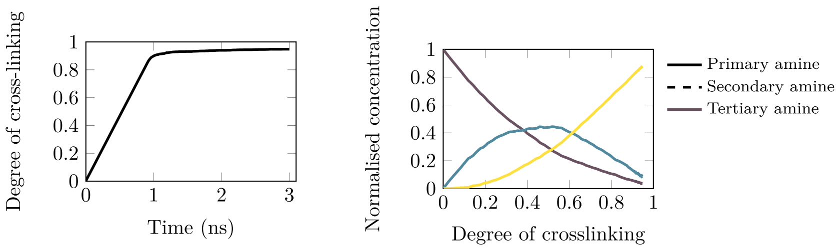

(a)

(b)

Fig. 7. Simulation results of the curing process: (a) Evolution of the degree of curing with simulation time, and (b) the relative change of reactive amine groups as a function of the degree of curing.

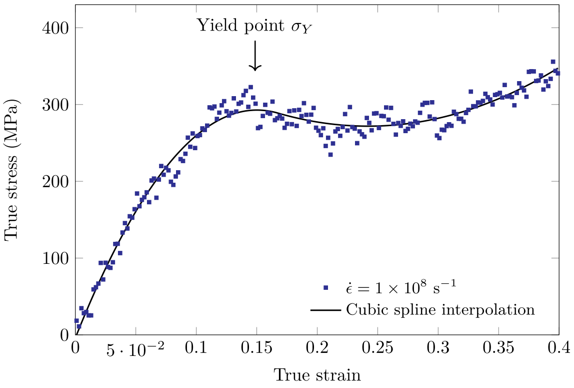

Fig. 9. Tensile stress-strain behavior of an cured epoxy system at strain rate $\dot{\epsilon} = 1 \times 10^8$ s^{-1}.

It is noteworthy that polymer network structures are ideally homogeneous in the simulations, while voids and cavities are created during the synthesis process of polymer materials. The presence of voids in polymer composites results in reductions in the matrix-dominated mechanical properties. Therefore, the evolution of damage state measured from experimental tests is different with that obtained using MD simulations. Therefore, in order to take into account the damage behavior in the composite polymers, a phenomenological damage model presented in Eq. (35) is considered. The damage model is calibrated using uniaxial tensile tests as discussed later. All the simulations are performed with the Large-scale Atomic/Molecular Massively Parallel Simulator (LAMMPS) [53].

3.3. Modeling of cured epoxy under shear loading

As discussed in Section 2, the connectivity and stretching of the polymer network impart the hyperelastic behavior and a generalized neo-Hookean model presented in Eq. (28) captures this behavior. Here, we present a MD simulation-based method to analyze the long-term configuration change of cured epoxy polymer subjected to a shear deformation. It allows us to study the stress relaxation behavior of the epoxy under a constant strain and to capture the time-independent response of the epoxy by which the corresponding time-independent shear modulus of the material that is required in Eq. (28) is obtained.

Shear strains of 1% are initially applied to the cured samples in the xy-, yz-, and xz-planes. The simulation box is deformed at a strain rate of 10^7 s^{-1} and room temperature under NPT ensemble to control normal stresses along the x-, y- and z-directions at zero. To study the long-term response of the material, we utilized a method similar to that recently introduced to simulate an artificial relaxation [54]. In this method, starting from the deformed configuration, the system is subjected to small cyclic perturbations of tensile/compressive stresses along the x-, y- and z-directions $\pm\sigma_p$ around zero pressure, while the shear strain is held constant. The cyclic stresses with period 100 ps are applied to the polymer system using a series of NPT simulations at room temperature. Fig. 11 shows a cyclic tensile/compressive stresses at $\sigma_p = \pm 200$ MPa. These small perturbations of stresses allow the system to overcome energy barriers to atomic motion in a computationally feasible time scale. The shear stress is averaged over a number of the cycles. It is worth noting that the relaxation process does not depend on the choice of σ_p [54] since the sum of the cyclic stresses is zero over the cycles.

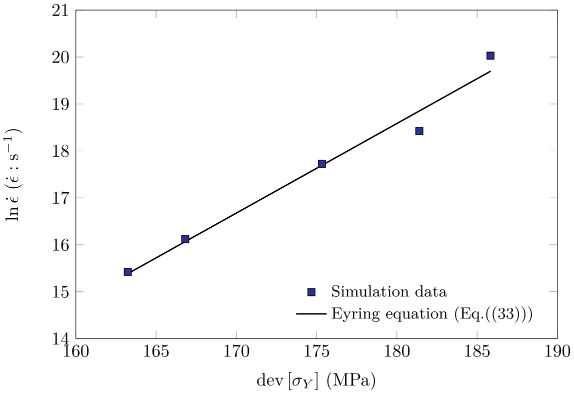

Fig. 10. Strain rate dependence of the yield stress.

Fig. 12a–c presents the variation of the shear modulus with respect to the number of stress perturbation cycles applied to three different cured epoxy configurations. The simulation results show that although the trend of the artificial relaxation varies for different configurations, the shear modulus reaches a plateau at $\mu = 205 \pm 30$ MPa after up to 2000 of the cycles (i.e., 200 ns). The plateau represents the time-independent response of epoxy resin under shear loading. A piecewise linear curve with two optimal knots is fitted to the simulation data points to estimate the shear stress at the relaxed configuration.

4. Finite element analysis

Next, we use the constitutive model to develop a continuum mechanics incremental formulation of nonlinear problems with respect to finite element solution variables. It would make it possible to evaluate the applicability of the proposed atomistically informed constitutive model. In the following section, the continuum mechanics incremental and finite element equations are derived.

4.1. Total Lagrangian formulation

The motion of a general body is considered in a stationary Cartesian coordinate system and the aim is to evaluate the equilibrium positions of the body at the discrete time points $0, \Delta t, 2\Delta t, \ldots, t$ where Δt is an increment in time. The equilibrium of the body at time $t + \Delta t$ using the principle of virtual displacements is expressed as

$$\int_{t+\Delta t_V} {}^{t+\Delta t}T_{ij} \delta^{t+\Delta t} e_{ij} d^{t+\Delta t} V = {}^{t+\Delta t}\mathscr{R} -, \tag{37}$$

where ${}^{t+\Delta t}T_{ij}$ is the Cauchy stress tensor, ${}^{t+\Delta t}e_{ij}$ is strain tensor corresponding to virtual displacement, ${}^{t+\Delta t}V{+}\Delta t$ is volume at time $t+\Delta t$, and ${}^{t+\Delta t}\mathscr{R}{+}\Delta t$ is the external virtual work.

Eq. (37) cannot be solved directly since the configuration at time $t + \Delta t$ is unknown. A solution to the equation is obtained by referring all variables to the initial configuration at time 0 of the body that is called the total Lagrangian (TL) formulation. In the formulation, we consider the following equilibrium equation for the body in the configuration at time $t + \Delta t$

$$\int_{0_V} {}^{t+\Delta t}_{0}S_{ij} \delta^{t+\Delta t}_{0} \varepsilon_{ij} d^0 V = {}^{t+\Delta t}\mathscr{R}, \tag{38}$$

where $0^{t+\Delta t}S_{ij}$ is the 2nd Piola-Kirchhoff stress tensor, $0^{t+\Delta t}\varepsilon_{ij}$ is the Green-Lagrange strain tensor. and the deformation-independent loading ${}^{t+\Delta t}\mathscr{R}{+}\Delta t$ is given by

$${}^{t+\Delta t}\mathscr{R} = \int_{0_A} {}^{t+\Delta t}_{0}f^s_i \delta u_i d^0 A + \int_{0_V} {}^{t+\Delta t}_{0}f^b_i \delta u_i d^0 V \mathscr{R} \tag{39}$$

The linearized equilibrium equation in the TL formulation is then obtained

$$\int_{0_V} {}_0C_{ijrs0}e_{rs} \delta_0 e_{ij} d^0 V + \int_{0_V} {}^{t}_{0}S_{ij} \delta\delta_0 \eta_{ij} d^0 V = {}^{t+\Delta t}\mathscr{R} - \int_{0_V} {}^{t}_{0}S_{ij} \delta\delta_0 e_{ij} d^0 V, \tag{40}$$

where ${}_0e_{ij}$ and ${}_0\eta_{ij}$ are the linear and nonlinear incremental strains which

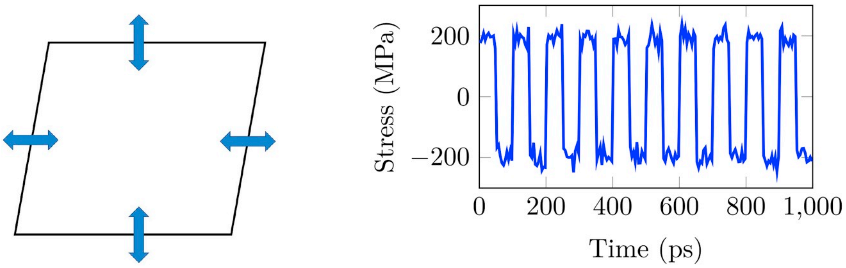

Fig. 11. Schematic illustration of the cyclic perturbations of tensile/compressive stresses at a constant shear strain (left), and Loading/unloading cycles versus time (right).

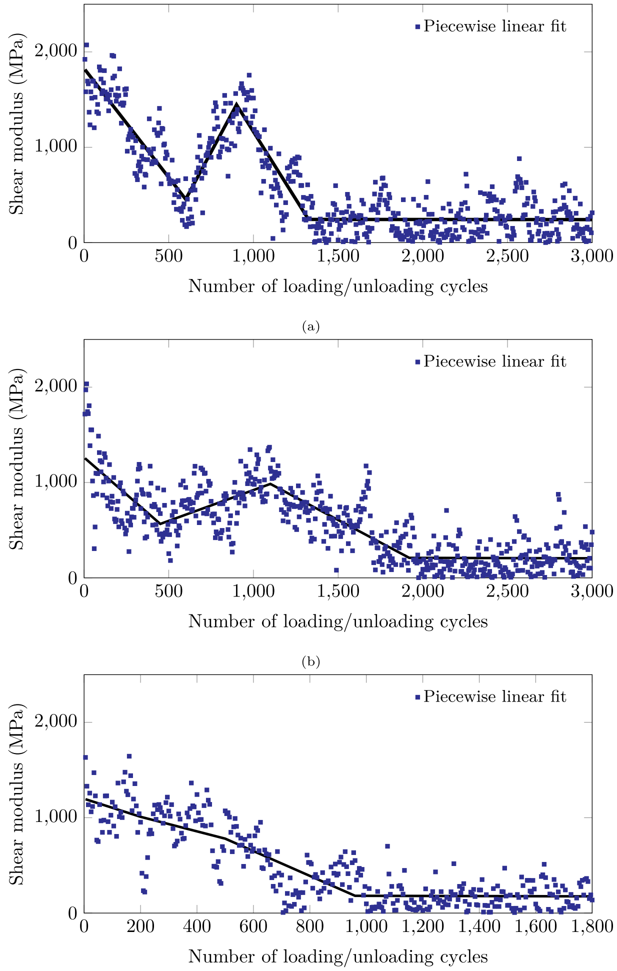

(a)

(b)

(c)

Fig. 12. (a)–(c) Shear modulus with respect to the number of loading/unloading cycles at $\sigma_p = 200$ MPa and room temperature. The initial shear strain is 0.01.

are referred to the configurations at times 0.

${}_{0}C_{ijrs}$ is the incremental stress-strain tensors at time t referred to the configurations at time 0, which is obtained from the constitutive model presented in Section 2. However, a closed-form calculation of the tensor for the constitutive model is not a straightforward task. Here, we follow a numerical perturbation method to derive an approximate tangent stiffness matrix [55]. Since the constitutive model uses a TL formulation, the derivative of the stress increment function $\Delta\sigma$ with respect to the strain increment tensor $\Delta\varepsilon$ takes the following form

$$\frac{\partial\Delta\sigma}{\partial\Delta\varepsilon} \cong \frac{\delta\Delta\sigma}{\delta\Delta\varepsilon} = \frac{{}^{t+\Delta t}\sigma\left({}^{t}_{0}F^{e}, {}^{t}_{0}F^{i}, {}^{t+\Delta t}_{0}\tilde{F}\right) - {}^{t+\Delta t}\sigma\left({}^{t}_{0}F^{e}, {}^{t}_{0}F^{i}, {}^{t+\Delta t}_{0}F\right)}{\delta}, \tag{41}$$

where ${}^{t+\Delta t}_{0}\tilde{F}{+}\Delta t$ is the perturbated deformation gradient and δ is the size of the perturbation. For a three-dimensional analysis, the deformation gradient ${}^{t+\Delta t}_{0}F{+}\Delta t$ must be perturbated six times to derive the Jacobian matrix. The reader is referred to Ref. [55] for a detailed discussion on the numerical approximation of the tangent stiffness matrix.

4.2. Finite element matrices

Displacements are then discretized at the element level using $\mathbf{u}^h = \mathbf{N}\mathbf{u}$, where the shape function matrix $\mathbf{N}$ interpolates the nodal values $\mathbf{u}$. Substituting the element coordinates and displacement interpolations into Eq. (40), the following system of equations for a single element is obtained:

$$({}^{t}_{0}\mathbf{K}_L + {}^{t}_{0}\mathbf{K}_{NL})\mathbf{u} = {}^{t+\Delta t}\mathbf{R} - {}^{t}_{0}\mathbf{F}, \tag{42}$$

where ${}^{t}_{0}\mathbf{K}_L$ and ${}^{t}_{0}\mathbf{K}_{NL}$ are the linear and nonlinear strain (geometric) incremental stiffness matrices, respectively. ${}^{t+\Delta t}\mathbf{R}{+}\Delta t$ is the vector of externally applied nodal point loads at time $t+\ \Delta t$; ${}^{t}_{0}\mathbf{F}$ is the vector of nodal point forces equivalent to the element stresses at time t; and $\mathbf{u}$ is the vector of increments in the nodal point displacements. The stiffness matrices and force vectors are obtained from the finite element evaluation as

$${}^{t}_{0}\mathbf{K}_L = \int_{{}^{0}\mathbf{V}} {}^{t}_{0}\mathbf{B}^{T}_{L}\,{}_{0}\mathbf{C}\,{}^{t}_{0}\mathbf{B}_L\, d^{0}V, \tag{43}$$

$${}^{t}_{0}K_{NL} = \int_{0_V} {}^{t}_{0}\mathbf{B}^{T}_{NL}\,{}^{t}_{0}\mathbf{S}\,{}^{t}_{0}\mathbf{B}_{NL}\, d^{0}V, \tag{44}$$

$${}^{t+\Delta t}\mathbf{R} = \int_{0_A} \mathbf{N}^{A^T}\,{}^{t+\Delta t}_{0}\mathbf{f}^{s}\, d^{0}A + \int_{0_V} \mathbf{N}^{T}\,{}^{t+\Delta t}_{0}\mathbf{f}^{b}\, d^{0}V, \tag{45}$$

$${}^{t}\mathbf{F} = \int_{0_V} {}^{t}_{0}\mathbf{B}^{T}_{L}\,{}_{0}\overset{t}{\widehat{\mathbf{S}}}\, d^{0}V, \tag{46}$$

where ${}^{t}_{0}\mathbf{B}_L$ and ${}^{t}_{0}\mathbf{B}_{NL}$ are the linear and nonlinear strain-displacement transformation matrices, ${}_{0}\mathbf{C}$ is the incremental material property matrix, ${}^{t}_{0}\mathbf{S}$ is a matrix of 2nd Piola-Kirchhoff stresses, and ${}_{0}\overset{t}{\widehat{\mathbf{S}}}$ is a vector of these stresses. All the matrices are defined at time t with respect to the configuration at time 0.

The linearization presented in Eq. (40) introduce errors leading to solution instability. It is therefore necessary to iterate in each load step until the relative L_2-norm of the residual in Eq. (38) is less than a given tolerance set as 10^{-5}. The equilibrium iterations corresponding to a modified Newton iteration in the TL formulation is

$$({}^{t}_{0}\mathbf{K}_L + {}^{t}_{0}\mathbf{K}_{NL})\Delta\mathbf{u}^{(i)} = {}^{t+\Delta t}\mathbf{R} - {}^{t+\Delta t}_{0}\mathbf{F}^{(i-1)}.(i = 1, 2, 3\ldots) \tag{47}$$

Table 3 summarizes a step-by-step algorithm used to the system of non-linear equations presented in Eq. (47).

5. Results and discussion

As discussed earlier in sections 2 and 3, the material parameters associated with the hyperelastic spring (i.e., μ_M^{he}) and viscoelastic dashpot elements (i.e., $\dot{\varepsilon}_0$ and V^*) are determined using MD simulations. Further to the atomistically measured parameters, those of the nonlinear elastic spring (i.e., μ_M^e and λ_M^e), the damage variable (i.e., A) and the fiber parameters (i.e., a_1, a_2 and a_3) are obtained through a calibration process with experimental data. In this study, commercially available spray dried BNPs with a primary particle size of 14 nm (DISPERAL HP14, SASOL [56]) and GFs with an average diameter and length of 11.5 and 350 μm (FG 300 [57]) are used, respectively. The mass density of the neat epoxy, BNP and GF are respectively 1.2, 3.0 and 2.55 g/cc from which the BNP and GF volume fractions required in the constitutive model can be obtained. Nanoparticles have a tendency to undergo agglomeration. The aggregation of nanoparticles results in insufficient dispersal in the polymer matrix, degrading the material properties of the nanocomposites. To reduce the particle agglomeration by shear mixing process, BNPs are dispersed in the epoxy using a high-energy vacuum dissolver at an extremely high rotation speed of 5800 rpm. The dissolver provides high shear forces to break up the agglomerates in the liquid epoxy in vacuum. The GFs are dispersed in the epoxy with a moderate rotation speed in order to avoid breakage of the fibers. The nanocomposites are prepared by firstly dispersing the required amount of BNPs in the liquid epoxy and by subsequent introduction of the fibers in the BNP-filled epoxy compound. Afterwards, the compound is blended with the curing agents. Finally, the material is cast in a preheated (80 C) casting tool (depending on the test method, a size of nearly DIN A4 with thicknesses between 2 and 5 mm) and cured for 4 h at 80 C for gelation and 4 h at 120 C for post-curing. The casting tool is made of stainless steel and to provide an easy release a water-based mold release system is used.

Table 3
Summary of step-by-step algorithm used for FE analysis.

1. The value of tensors $\{{}^{t}_{0}\mathbf{F},{}^{t}_{0}\mathbf{F}_e,{}^{t}_{0}\mathbf{F}_v,{}^{t+\Delta t}_{0}\mathbf{F}+\Delta t\}$ is available at the beginning of each time increment.
2. Calculate the trial elastic deformation gradient using Eq. (1)
$${}^{t+\Delta t}_{0}\mathbf{F}_e^{trial} = {}^{t+\Delta t}_{0}\mathbf{F}+\Delta t\,{}^{t}_{0}\mathbf{F}_v^{-1}.$$
3. Perform the polar decomposition
$${}^{t+\Delta t}_{0}\mathbf{F}_e^{trial} = {}^{t+\Delta t}_{0}\mathbf{V}_e^{trial}\,{}^{t+\Delta t}_{0}\mathbf{R}_e^{trial}.$$
4. Compute the trial elastic strain
$${}^{t+\Delta t}_{0}\mathbf{E}_e^{trial} = \sum_{i=1}^{3}(\ln \lambda_{trial}^{(i)})\mathbf{e}_{trial}^{(i)} \otimes \mathbf{e}_{trial}^{(i)},$$
where $\lambda_{trial}^{(i)}$ and $\mathbf{e}_{trial}^{(i)}$ are the eigenvalues and eigenvectors of ${}^{t+\Delta t}_{0}\mathbf{V}_e^{trial}$.
5. Calculate the trail stress ${}^{t+\Delta t}\mathbf{T}_{neq}^{trial}6$ using Eq. (29).
6. Calculate the deviatoric part of ${}^{t+\Delta t}\mathbf{T}_{neq}^{trial}$.
7. Calculate the trial viscoelastic flow rate $\dot{\varepsilon}_{trial}^{v}$ using Eq. (33).
8. Calculate the trial viscoelastic stretching $\mathbf{D}_v^{trial}$ from Eq. (32).
9. Update ${}^{t+\Delta t}_{0}\mathbf{F}_v$ using the backward Euler method and Eq. (34)
$${}^{t+\Delta t}_{0}\mathbf{F}_i = {}^{t}_{0}\mathbf{F}_i + \Delta t\mathbf{D}_i^{trial}\,{}^{t+\Delta t}_{0}\mathbf{F}_i^{trial},$$
where Δt is the time increment and ${}^{t+\Delta t}_{0}\mathbf{F}_i^{trial} = \left({}^{t+\Delta t}_{0}\mathbf{F}_e^{trial}\right)^{-1}\,{}^{t+\Delta t}_{0}\mathbf{F}+\Delta t$.
10. If $\left|\left|{}^{t+\Delta t}_{0}\mathbf{F}_v - {}^{t+\Delta t}_{0}\mathbf{F}_i^{trial}\right|\right| <$ tolerance then GOTO step 11 else GOTO step 2.
11. Calculate ${}^{t+\Delta t}_{0}\mathbf{T}_{eq}$ using Eq. (28).
12. Calculate the damage variable at $t+\Delta t$ using Eq. (35).
13. With ${}^{t+\Delta t}_{0}\mathbf{T}_{qe}$, ${}^{t+\Delta t}_{0}\mathbf{T}_{nqe}$ and d obtained in previous steps calculate the total stress using Eq. (27).
14. Store ${}^{t+\Delta t}_{0}\mathbf{F}_e$ and ${}^{t+\Delta t}_{0}\mathbf{F}_i$ and report the total stress ${}^{t+\Delta t}_{0}\mathbf{T}+\Delta t$.
15. Compute of the tangent stiffness matrix using Eq. (41).
16. Solve the system of non-linear equations presented in Eq. (47) using the Newton-Raphson procedure.

The state of damage and the tangent stiffness matrix are updated at each Newton-Raphson iteration.

GFs are in-plane randomly-oriented, which are represented by two families of fibers with the initial fiber directions of $\mathbf{a}_0^1 = [1 \quad 0 \quad 0]$ and $\mathbf{a}_0^2 = [0 \quad 1 \quad 0]$. In the following section, the constitutive model is first calibrated based on a comparison with tensile test results of neat epoxy, BNP/epoxy nanocomposites and GF/epoxy composites. The predictive capabilities of the calibrated model to predict the stress-strain response of GF reinforced BNP/epoxy nanocomposites is then validated by experimental data. Next, the model is implemented in the FEA and is validated by comparing the numerical and experimental results of a four-point bending test.

5.1. *Experimental parameters identification*

The objective of this section is to identify the aforementioned material parameters using experimental data obtained from uniaxial tensile tests. Concerning the tensile tests, specimens with a thickness of 2.2 mm are produced and tested according to testing standard DIN EN ISO 527-2, using an extensometer to measure the elongation of samples (Fig. 13). The specifications of the specimens are highlighted in Fig. 14. The stress-strain curves are recorded with a test speed of 2 mm/min.

To calibrate the material parameters, the stress-strain relationships of three types of specimens made of neat epoxy, BNP (20 wt%)/epoxy nanocomposites and GF (60 wt%)/epoxy composites obtained from the constitutive model is compared with those of experimental data. An object function of differences between model results and experimental data is numerically minimized using the single-objective genetic algorithm method available in the DAKOTA software package [58]. The experimentally identified parameters of the constitutive model are listed in Table 4. These parameters are obtained with ten experimental tests at engineering strain rate $\dot{\varepsilon} = 2.90 \times 10^{-4}\ \mathrm{s}^{-1}$ and room temperature.

Based on the material parameters presented in Tables 2 and 4, the stress-strain relationship can be obtained from equations presented in section 2. Fig. 15 presents the model predictions for neat epoxy, BNP (20 wt%)/epoxy nanocomposites and GF (60 wt%)/epoxy composites compared with experimental data. The mean values and standard deviations of the data calculated from ten uniaxial tensile tests are shown in the figure. The simulation results show that the proposed constitutive model is able to fairly predict the stress-strain behavior of nanoparticle and fiber reinforced epoxy.

It should be noted that the parameters identification procedure adopted here aims to provide a unique set of material parameters for GF reinforced BNP/epoxy nanocomposites. The predictive capability of the constitutive model with the unique set of parameters is further evaluated in the next section.

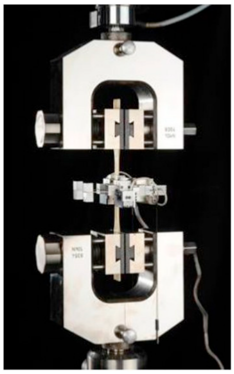

Fig. 13. Experimental setup for tensile test of the nanocomposite specimens with extensometer to measure the elongation of the samples.

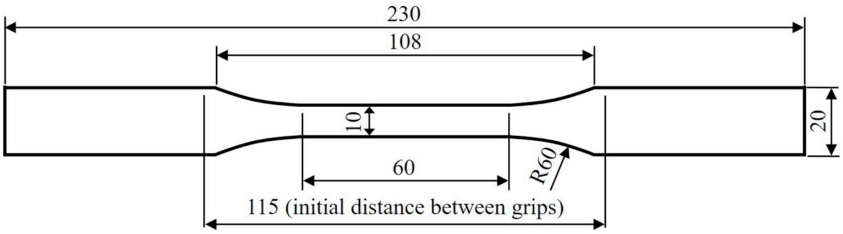

Fig. 14. Planar dimensions of the specimens with a thickness of 2 mm used for tensile tests. All dimensions are in millimeters.

Table 4
Material parameters identified by experimental tests.

Parameter	Equation	Value
μ_M^e (MPa)	(29)	810
λ_M^e (MPa)	(29)	1100
A	(35)	200
a_1	(35)	9
a_2	(35)	1
a_3	(35)	1

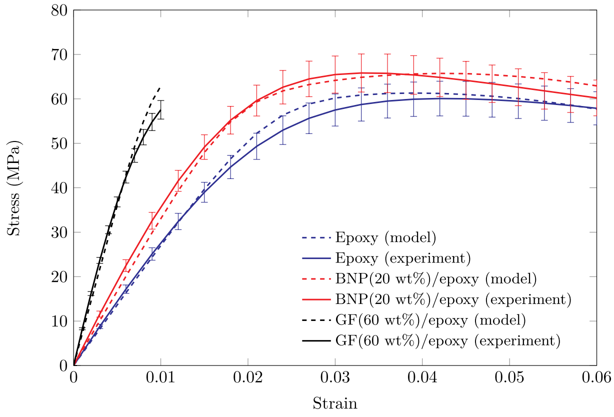

Fig. 15. Stress-strain curves of reinforced epoxy resin at strain rate $\dot{\varepsilon} = 1.54 \times 10^{-4}\ \mathrm{s}^{-1}$ and room temperature under uniaxial tensile loading. The mean values and standard deviations of the experimental data are obtained from ten uniaxial tests.

5.2. Model validation

The second investigation here considered deals with a series of uniaxial tensile tests of GF reinforced BNP/epoxy nanocomposites. It allows us to evaluate the model performance in predicting the stress-strain relationship of the nanocomposites in the simultaneous presence of GF and BNP reinforcements with the calibrated material parameters listed in Tables 4 and 2

Fig. 16 shows the effect of GF and BNP weight fractions on the stress-strain behavior at $\dot{\varepsilon} = 1.54 \times 10^{-4}\ \mathrm{s}^{-1}$ and room temperature under uniaxial tensile loading. Both experimental and numerical results are presented in the figure. From the experimental data, the Young's modulus increases from 2.95 to 4.10 GPa for neat epoxy and BNP (20 % wt)/epoxy nanocomposites, respectively. The Young's modulus respectively increases to 4.75, 5.25 and 7.07 GPa by increasing the GF weight fraction from 15 to 30 and 60 wt%, indicating percentage increases of 61, 78 and 140%, respectively. The results show that the ductile behavior of the nanocomposites significantly affected by the fibers such that the critical strain decreases from 0.06 for neat polymer to 0.01 for GF (60 %wt)/epoxy composite. From Fig. 16, an overall satisfactory level of accuracy between the proposed model and the experimental data can be observed, evidencing the practicability and representativeness of the developed constitutive model at different GF and BNP weight fractions. There are some discrepancies between the model prediction and experimental data, which might be caused by the unique set of material parameters and the free energy terms defined in Eqs. (24) and (25). Fig. 17 shows the evolution of the damage variable d during this deformation course for the neat epoxy material, showing a monotonically increasing trend with strain.

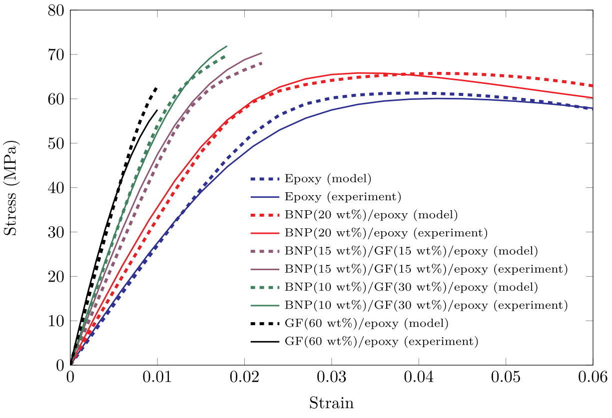

Fig. 16. Effect of GF and BNP weight fraction on the stress-strain relationship of the nanocomposites at strain rate $\dot{\varepsilon} = 1.54 \times 10^{-4}\ \mathrm{s}^{-1}$ and room temperature under uniaxial tensile loading. The mean values and standard deviations of the experimental data are obtained from ten uniaxial tests.

5.3. Application of the proposed model

Finally, a four-point bending test of a beam made of GF reinforced BNP/epoxy nanocomposites is analyzed to examine the predictive capability of the developed constitutive model in a real application. The bending tests are performed according to DIN EN ISO 14125 at a

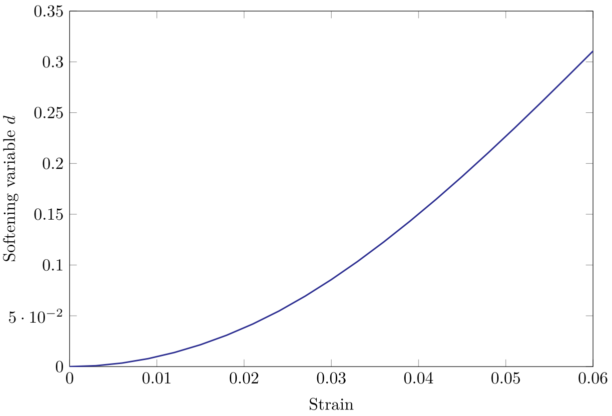

Fig. 17. Evolution of the softening variable d with strain for the neat epoxy.

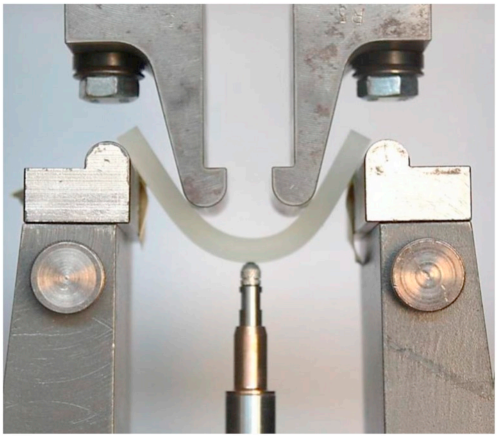

Fig. 18. Experimental setup for four-point bending test.

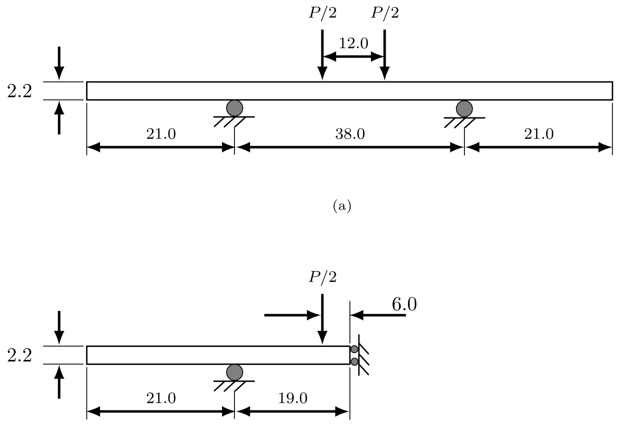

(a)

(b)

Fig. 19. Four-point bending test: (a) geometry of the specimen and boundary conditions, (b) loading and boundary conditions imposed on half of the beam because of symmetry. The specimen thickness is 10.1 mm. All dimensions are in millimeters.

Fig. 20. Two-dimensional finite element model composed of 1064 Q4 elements with 1187 nodes.

constant speed of 2 mm/min and an initial load of 5 N, while load and displacement are recorded (see Fig. 18). The specifications of the specimens tested in the investigation are illustrated in Fig. 19a. The width of the specimens is 10.1 mm.

Due to the specimen symmetry, a FEA of half of the beam using symmetric boundary conditions would provide as complete a solution as that of the full model with less computational cost. The reduced model takes into account the symmetry at the mid-length of the specimen as illustrated in Fig. 19b. Fig. 20 shows the corresponding finite element mesh with 1187 nodes and 1064 four-noded quadrilateral (Q4) elements. The mesh is refined toward the right side of the model because of high stress and strain concentrations in the area. The following simulations are performed under plane strain conditions and the load is applied via an imposed displacement at a constant rate of 2 mm/min.

Fig. 21 shows the numerical predictions of the four-point bending tests of samples made of neat epoxy and different combinations of the GF and BNP weight fraction. The numerical results are compared with experimental data. The mean values and standard deviations of the data calculated from ten four-point bending tests are presented in the figure. From the resulting force-displacement curves, it can be seen that the flexural resistance increases by incorporating the GF and BNP content in the epoxy matrix.

The flexural modulus can be calculated from the linear portion of the curves by determining the load F and its corresponding displacement d as $E_f = \frac{23}{108}\frac{FL^3}{wt^3d}$, where L, w and t are the loading span, the width and thickness of the specimen, respectively. The numerical results indicate that the flexural modulus increases from 3.61 GPa for neat epoxy to 5.32 GPa for BNP(20 wt%)/epoxy, showing a percentage increase of 47%. The flexural modulus further increases to 7.28 and 9.67 GPa by increasing the GF weight fraction to 15 and 60 wt%, respectively. The numerical results are consistent with experimental data. The resulting force-displacement curves clearly indicate a satisfactory level of agreement along the whole evolution, which again evidences the ability of the proposed constitutive model in predicting the rate-dependent behavior of GF reinforced BNP/epoxy nanocomposites.

Finally, Fig. 22 shows the evolution of the damaged zone. Figs.. 22a and b correspond to imposed displacements of 3.0 and 4.0 mm, respectively. It is worth noting that the material softening is modeled using damage variables. Beyond the onset of softening, strain localization happens in the classical continuum damage model, which leads to the loss of solution uniqueness [59,60]. Consequently, the numerical solution obtained from the FEA will be mesh-dependent. To avoid the well-known problem, we only continue the finite element solutions before the onset of stress softening at Gauss points.

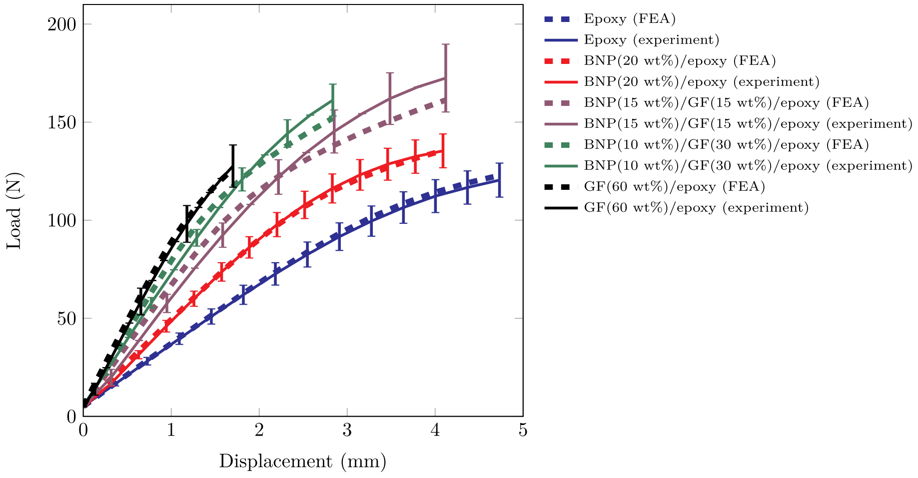

Fig. 21. Effect of the GF and BNP weight fraction on the force-displacement response in the four-point bending test of the nanocomposites.

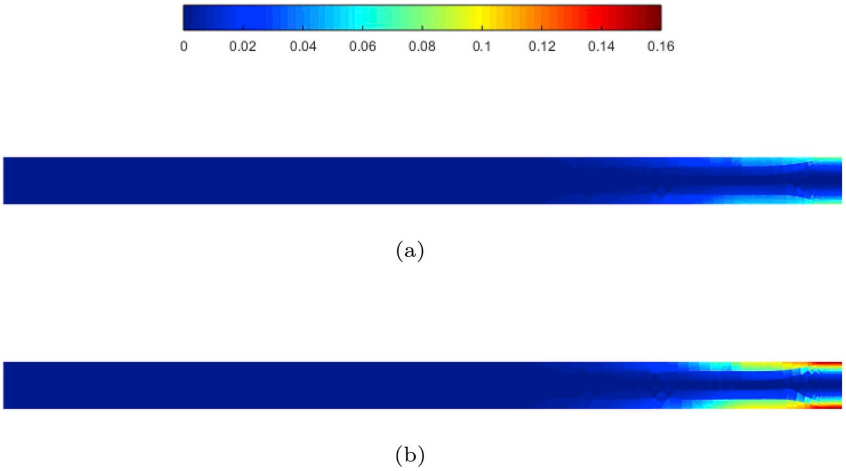

(a)

(b)

Fig. 22. Contour plots of damage (d) for 1064 Q4 elements and imposed displacement of (a) 3 mm, and (b) 4 mm.

6. Summary and conclusions

A physically based constitutive model accounting for the nonlinear hyperelastic, time-dependent and softening behavior of GF reinforced BNP/epoxy nanocomposites at finite strain was proposed. The model adopts a composite-based hyperelastic model and a modulus enhancement model to take into account the effect of the fiber and nanoparticle weight fraction on the stress-strain relationship. The softening behavior was modeled by an internal variable, which is assumed to obey a saturation type evolution rule.

A methodological framework based on MD simulations and experimental tests was developed to calibrate the proposed model. For this, MD simulations were performed to investigate the rate-independent equilibrium and rate-dependent viscoelastic material behavior of epoxy resins. Molecular simulations of epoxy resins under tensile loading at various strain rates allowed the identification of viscoelastic material parameters (i.e., $\dot{\varepsilon}_0$ and V^*) required for the Eyring model. A MD simulation-based method was also presented to study the equilibrium response of epoxy resin subjected to shear loading. It enabled predicting the hyperelastic material parameters (i.e., μ_M^{he}). Further to the atomistically predicted parameters, uniaxial tensile tests of GF and BNP reinforced epoxy were conducted to identify the elastic spring and softening and fiber parameters (i.e., $\mu_M^e, \lambda_M^e, A, a_1, a_2$ and a_3).

The predictive capability of the constitutive model with the unique set of parameters for different fiber and nanoparticle contents was evaluated. The comparison of simulation results of uniaxial tensile tests at room temperature with experimental data confirms that the model is able to adequately capture the overall material behavior of GF reinforced BNP/epoxy nanocomposites. The applicability of the model was demonstrated through its implementation in the FEA of four-point bending tests. Experimental-numerical validation showed a satisfactory level of accuracy along the loading evolutions.

It is worth noting that the proposed constitutive model predicts the stress-strain relationships at room temperature. In the future, it would be interesting to study the effect of temperature on the material behavior of the nanocomposites. The potential development would provide a more comprehensive model to better understand the thermoviscoelastic behavior of the nanocomposites. Furthermore, more experimental tests than those reported in this study are still required to see if the present model can predict the hysteresis behavior under cyclic loading. Finally, the present modeling framework can be equipped with coarse-grained force fields [61,62] to allow simulations of polymer systems at larger length and time scales.

Acknowledgments

This work originates from the research project ‘Hybrid laminates and nanoparticle reinforced materials for improved rotor blade structures’ (‘LENAH - Lebensdauererhöhung und Leichtbauoptimierung durch nanomodifizierte und hybride Werkstoffsysteme im Rotorblatt’), funded by the Federal Ministry of Education and Research of Germany. The authors wish to express their gratitude for the financial support.

References

[1] Uddin MF, Sun C. Strength of unidirectional glass/epoxy composite with silica nanoparticle-enhanced matrix. Compos Sci Technol 2008;68(7–8):1637–43.
[2] Fu S-Y, Feng X-Q, Lauke B, Mai Y-W. Effects of particle size, particle/matrix interface adhesion and particle loading on mechanical properties of particulate–polymer composites. Compos B Eng 2008;39(6):933–61.
[3] Shahid N, Villate RG, Barron AR. Chemically functionalized alumina nanoparticle effect on carbon fiber/epoxy composites. Compos Sci Technol 2005;65(14):2250–8.
[4] Chen W, Wu S, Lei Y, Liao Z, Guo B, Liang X, Jia D. Interfacial structure and performance of rubber/boehmite nanocomposites modified by methacrylic acid. Polymer 2011;52(19):4387–95.
[5] Jux M, Fankhänel J, Daum B, Mahrholz T, Sinapius M, Rolfes R. Mechanical properties of epoxy/boehmite nanocomposites in dependency of mass fraction and surface modification-An experimental and numerical approach. Polymer 2018;141:34–45.
[6] Krairi A, Doghri I. A thermodynamically-based constitutive model for thermoplastic polymers coupling viscoelasticity, viscoplasticity and ductile damage. Int J Plast 2014;60:163–81.
[7] Bardella L. A phenomenological constitutive law for the nonlinear viscoelastic behaviour of epoxy resins in the glassy state. Eur J Mech A Solid 2001;20(6):907–24.
[8] Diab H, Wu Z. Nonlinear constitutive model for time-dependent behavior of FRP-concrete interface. Compos Sci Technol 2007;67(11–12):2323–33.
[9] Vogler M, Rolfes R, Camanho P. Modeling the inelastic deformation and fracture of polymer composites–Part I: plasticity model. Mech Mater 2013;59:50–64.
[10] Nguyen V-D, Lani F, Pardoen T, Morelle X, Noels L. A large strain hyperelastic viscoelastic-viscoplastic-damage constitutive model based on a multi-mechanism non-local damage continuum for amorphous glassy polymers. Int J Solids Struct 2016;96:192–216.
[11] Mlyniec A, Korta J, Uhl T. Structurally based constitutive model of epoxy adhesives incorporating the influence of post-curing and thermolysis. Compos B Eng 2016;86:160–7.
[12] Park H, Choi J, Kim B, Yang S, Shin H, Cho M. Toward the constitutive modeling of epoxy matrix: temperature-accelerated quasi-static molecular simulations consistent with the experimental test. Compos Part B 2018;142(1):131–41.
[13] Bardenhagen SG, Stout MG, Gray GT. Three-dimensional, finite deformation, viscoplastic constitutive models for polymeric materials. Mech Mater 1997;25(4):235–53.
[14] Zaïri F, Naït-Abdelaziz M, Woznica K, Gloaguen J-M. Constitutive equations for the viscoplastic-damage behaviour of a rubber-modified polymer. Eur J Mech A Solid 2005;24(1):169–82.
[15] Pyrz M, Zairi F. Identification of viscoplastic parameters of phenomenological constitutive equations for polymers by deterministic and evolutionary approach. Model Simul Mater Sci Eng 2007;15(2):85.

[16] Khajehsaeid H, Arghavani J, Naghdabadi R, Sohrabpour S. A visco-hyperelastic constitutive model for rubber-like materials: a rate-dependent relaxation time scheme. Int J Eng Sci 2014;79:44–58.

[17] Poulain X, Benzerga A, Goldberg R. Finite-strain elasto-viscoplastic behavior of an epoxy resin: experiments and modeling in the glassy regime. Int J Plast 2014;62:138–61.

[18] Chebbi E, Wali M, Dammak F. An anisotropic hyperelastic constitutive model for short glass fiber-reinforced polyamide. Int J Eng Sci 2016;106:262–72.

[19] Boyce M, Socrate S, Llana P. Constitutive model for the finite deformation stress–strain behavior of poly (ethylene terephthalate) above the glass transition. Polymer 2000;41(6):2183–201.

[20] Boyce MC, Kear K, Socrate S, Shaw K. Deformation of thermoplastic vulcanizates. J Mech Phys Solids 2001;49(5):1073–98.

[21] Van Dommelen J v, Parks D, Boyce M, Brekelmans W, Baaijens F. Micromechanical modeling of the elasto-viscoplastic behavior of semi-crystalline polymers. J Mech Phys Solids 2003;51(3):519–41.

[22] Ahzi S, Makradi A, Gregory R, Edie D. Modeling of deformation behavior and strain-induced crystallization in poly (ethylene terephthalate) above the glass transition temperature. Mech Mater 2003;35(12):1139–48.

[23] Qi H, Boyce M. Stress–strain behavior of thermoplastic polyurethanes. Mech Mater 2005;37(8):817–39.

[24] Ayoub G, Zaïri F, Naït-Abdelaziz M, Gloaguen J. Modelling large deformation behaviour under loading–unloading of semicrystalline polymers: application to a high density polyethylene. Int J Plast 2010;26(3):329–47.

[25] Davidson JD, Goulbourne N. A nonaffine network model for elastomers undergoing finite deformations. J Mech Phys Solids 2013;61(8):1784–97.

[26] Miehe C, Göktepe S. A micro–macro approach to rubber-like materials. Part II: the micro-sphere model of finite rubber viscoelasticity. J Mech Phys Solids 2005;53(10):2231–58.

[27] Li Y, Tang S, Kröger M, Liu WK. Molecular simulation guided constitutive modeling on finite strain viscoelasticity of elastomers. J Mech Phys Solids 2016;88:204–26.

[28] Guo Z, Peng X, Moran B. A composites-based hyperelastic constitutive model for soft tissue with application to the human annulus fibrosus. J Mech Phys Solids 2006;54(9):1952–71.

[29] Guo Z, Peng X, Moran B. Large deformation response of a hyperelastic fibre reinforced composite: theoretical model and numerical validation. Compos Appl Sci Manuf 2007;38(8):1842–51.

[30] Peng X, Guo Z, Moran B. An anisotropic hyperelastic constitutive model with fiber-matrix shear interaction for the human annulus fibrosus. J Appl Mech 2006;73(5):815–24.

[31] Affdl JH, Kardos J. The Halpin-Tsai equations: a review. Polym Eng Sci 1976;16(5):344–52.

[32] Mullins L, Tobin N. Stress softenings in natural rubber vulcanizates, Part I. J Appl Polym Sci 1965;9:2993–3010.

[33] Mullins L. Softening of rubber by deformation. Rubber Chem Technol 1969;42(1):339–62.

[34] Govindjee S, Reese S. A presentation and comparison of two large deformation viscoelasticity models. J Eng Mater Technol 1997;119(3):251–5.

[35] Guth E. Theory of filler reinforcement. J Appl Phys 1945;16(1):20–5.

[36] Boyce MC, Parks DM, Argon AS. Large inelastic deformation of glassy polymers. Part I: rate dependent constitutive model. Mech Mater 1988;7(1):15–33.

[37] Ward IM, Sweeney J. Mechanical properties of solid polymers. John Wiley & Sons; 2012.

[38] Qi H, Boyce M. Constitutive model for stretch-induced softening of the stress–stretch behavior of elastomeric materials. J Mech Phys Solids 2004;52(10):2187–205.

[39] Miehe C, Keck J. Superimposed finite elastic–viscoelastic–plastoelastic stress response with damage in filled rubbery polymers. Experiments, modelling and algorithmic implementation. J Mech Phys Solids 2000;48(2):323–65.

[40] Blanchard A, Parkinson D. Breakage of carbon-rubber networks by applied stress. Rubber Chem Technol 1952;25(4):808–42.

[41] Bueche F. Molecular basis for the Mullins effect. J Appl Polym Sci 1960;4(10):107–14.

[42] Mullins L, Tobin N. Theoretical model for the elastic behavior of filler-reinforced vulcanized rubbers. Rubber Chem Technol 1957;30(2):555–71.

[43] Ju J, Lee H-K. A micromechanical damage model for effective elastoplastic behavior of partially debonded ductile matrix composites. Int J Solids Struct 2001;38(36–37):6307–32.

[44] Raghavan P, Ghosh S. A continuum damage mechanics model for unidirectional composites undergoing interfacial debonding. Mech Mater 2005;37(9):955–79.

[45] Budarapu PR, Gracie R, Yang S-W, Zhuang X, Rabczuk T. Efficient coarse graining in multiscale modeling of fracture. Theor Appl Fract Mech 2014;69:126–43.

[46] Talebi H, Silani M, Bordas SP, Kerfriden P, Rabczuk T. A computational library for multiscale modeling of material failure. Comput Mech 2014;53(5):1047–71.

[47] Talebi H, Silani M, Rabczuk T. Concurrent multiscale modeling of three dimensional crack and dislocation propagation. Adv Eng Software 2015;80:82–92.

[48] Martínez L, Andrade R, Birgin EG, Martínez JM. PACKMOL: a package for building initial configurations for molecular dynamics simulations. J Comput Chem 2009;30(13):2157–64.

[49] Nasdala L, Kempe A, Rolfes R. Are finite elements appropriate for use in molecular dynamic simulations? Compos Sci Technol 2012;72(9):989–1000.

[50] Mayo SL, Olafson BD, Goddard WA. DREIDING: a generic force field for molecular simulations. J Phys Chem 1990;94(26):8897–909.

[51] Unger R, Braun U, Fankhänel J, Daum B, Arash B, Rolfes R. Molecular modelling of epoxy resin crosslinking experimentally validated by near-infrared spectroscopy. Comput Mater Sci 2019;161:223–35.

[52] Eyring H. The activated complex in chemical reactions. J Chem Phys 1935;3(2):107–15.

[53] Plimpton S. Fast parallel algorithms for short-range molecular dynamics. J Comput Phys 1995;117(1):1–19.

[54] Yu Y, Wang M, Zhang D, Wang B, Sant G, Bauchy M. Stretched exponential relaxation of glasses at low temperature. Phys Rev Lett 2015;115(16):165901.

[55] I. Tomas, A. Cisilino, P. Frontini, Accurate, efficient and robust explicit and implicit integration schemes for the Arruda-Boyce viscoplastic model, Asociacion Argentina de Mecanica Computacional .

[56] Sasol. Dispersal HP14. Germany: Brunsbüttel; 2018. http://www.sasol.com.

[57] Textil-Werke Schwarzwälder. FG 300. Germany: Heinrich Kautzmann GmbH; 2018. http://www.stw-faser.de.

[58] B. M. Adams, W. Bohnhoff, K. Dalbey, J. Eddy, M. Eldred, D. Gay, K. Haskell, P. D. Hough, L. P. Swiler, Dakota, a multilevel parallel object-oriented framework for design optimization, parameter estimation, uncertainty quantification, and sensitivity analysis: version 5.0 user's manual, Sandia national laboratories, Tech Rep SAND2010-2183 .

[59] Bažant ZP, Jirásek M. Nonlocal integral formulations of plasticity and damage: survey of progress. J Eng Mech 2002;128(11):1119–49.

[60] Engelen RA, Geers MG, Baaijens FP. Nonlocal implicit gradient-enhanced elasto-plasticity for the modelling of softening behaviour. Int J Plast 2003;19(4):403–33.

[61] Mousavi AA, Arash B, Zhuang X, Rabczuk T. A coarse-grained model for the elastic properties of cross linked short carbon nanotube/polymer composites. Compos B Eng 2016;95:404–11.

[62] Arash B, Park HS, Rabczuk T. Coarse-grained model of the J-integral of carbon nanotube reinforced polymer composites. Carbon 2016;96:1084–92.